

# Title: Spin-orbit coupling controlled $J = 3/2$ electronic ground state in $5d^3$ oxides

**Authors:** A. E. Taylor,<sup>1</sup> S. Calder,<sup>1</sup> R. Morrow,<sup>2</sup> H. L. Feng,<sup>3</sup> M. H. Upton,<sup>4</sup>  
M. D. Lumsden,<sup>1</sup> K. Yamaura,<sup>3</sup> P. M. Woodward,<sup>2</sup> and A. D. Christianson<sup>\*1,5</sup>

<sup>1</sup>*Quantum Condensed Matter Division,*

*Oak Ridge National Laboratory, Oak Ridge, Tennessee 37831, USA*

<sup>2</sup>*Department of Chemistry, The Ohio State University, Columbus, Ohio 43210-1185, USA*

<sup>3</sup>*Research Center for Functional Materials,*

*National Institute for Materials Science,*

*1-1 Namiki, Tsukuba, Ibaraki 305-0044, Japan*

<sup>4</sup>*Advanced Photon Source, Argonne National Laboratory, Argonne, Illinois 60439, USA*

<sup>5</sup>*Department of Physics and Astronomy,*

*The University of Tennessee, Knoxville, TN 37996, USA*

*\*To whom correspondence should be addressed: Email: christiansad@ornl.gov*

**Abstract:** Entanglement of spin and orbital degrees of freedom drives the formation of novel quantum and topological physical states. Discovering new spin-orbit entangled ground states and emergent phases of matter requires both experimentally probing the relevant energy scales and applying suitable theoretical models. Here we report resonant inelastic x-ray scattering measurements of the transition metal oxides  $\text{Ca}_3\text{LiOsO}_6$  and  $\text{Ba}_2\text{YOsO}_6$ . We invoke an intermediate coupling approach that incorporates both spin-orbit coupling and electron-electron interactions on an even footing and reveal the ground state of  $5d^3$  based compounds, which has remained elusive in previously applied models, is a novel spin-orbit entangled  $J=3/2$  electronic ground state. This work reveals the hidden diversity of spin-orbit controlled ground states in  $5d$  systems and introduces a new arena in the search for spin-orbit controlled phases of matter.

**Main Text:** The electronic ground state adopted by an ion is a fundamental determinant of manifested physical properties. Recently, the importance of spin-orbit coupling (SOC) in creating the electronic ground state in  $5d$ -based compounds has come to the fore and

revealed novel routes to a host of unconventional physical states including quantum spin liquids, Weyl semimetals, and axion insulators (1, 2). As a result, major experimental and theoretical efforts have been undertaken seeking novel spin-orbit physics in various  $5d$  systems, and the influence of SOC has now been observed in the macroscopic properties of numerous systems. However, beyond the  $J_{\text{eff}} = 1/2$  case such as that found in  $\text{Sr}_2\text{IrO}_4$  (3) — which is a single-hole state that applies only to idealised  $5d^5$  ions in cubic materials — questions abound concerning the electronic ground states which govern  $5d$  ion interactions.

In this context  $5d^3$  materials present a particularly intriguing puzzle, because octahedral  $d^3$  configurations are expected to be orbitally-quenched  $S = 3/2$  states — in which case SOC enters only as a 3rd order perturbation (4) — yet there is clear experimental evidence that SOC influences the magnetic properties in  $5d^3$  transition metal oxides (TMOs). This includes the observations of large, SOC-induced spin-gaps in their magnetic excitation spectra (5–7) and x-ray absorption branching ratios which deviate from  $\text{BR} = I_{L3}/I_{L2} = 2$  (8, 9). Despite this, no description beyond the  $S = 3/2$  state had been established. The emergent phenomena in  $4d^3$  and  $5d^3$  systems, such as incredibly high magnetic transition temperatures (10–13), Slater insulators (14), and possible Mott-insulators (15) are therefore poorly understood.

We selected  $5d^3$  TMOs  $\text{Ca}_3\text{LiOsO}_6$  and  $\text{Ba}_2\text{YOsO}_6$  as model systems in which to investigate the influence of spin-orbit coupling on the electronic ground states via RIXS measurements on polycrystalline samples. Both materials have relatively-high magnetic ordering temperatures,  $T_N = 117$  and  $67$  K, respectively, despite large separation of nearest-neighbour Os ions of  $5.4$ – $5.9$  Å (5, 10, 16). The relative isolation of Os-O octahedra allows us to unambiguously access the ground state, because only extended superexchange interactions are present. Stronger, close-range interactions can mask the effective single-ion levels we wish to observe (17). In  $\text{Ca}_3\text{LiOsO}_6$  the oxygen octahedra surrounding  $\text{Os}^{5+}$  ions are very close to ideal, despite the overall non-cubic symmetry — hexagonal  $R\bar{3}c$  (10). As previously reported (5), we find that  $\text{Ba}_2\text{YOsO}_6$  has the ideal cubic double perovskite structure  $Fm\bar{3}m$  to within experimental measurement limits, see supplementary material for high-resolution

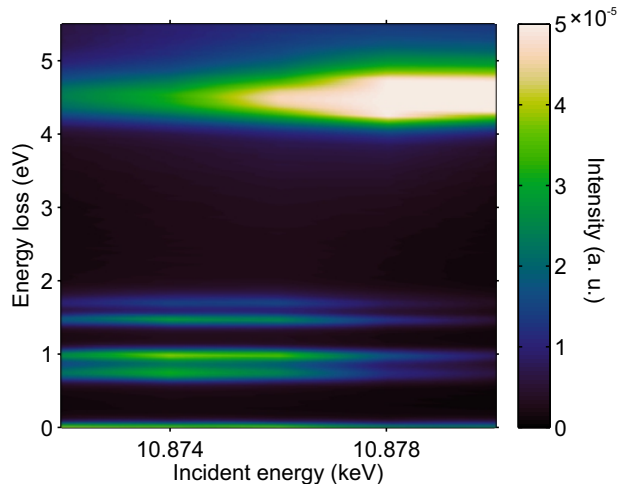


Figure 1: Incident energy dependence of electronic excitations in  $\text{Ca}_3\text{LiOsO}_6$ . Measurements were performed at 300 K.

synchrotron x-ray and neutron diffraction.

Figure 1 presents the x-ray energy loss,  $E$ , versus incident energy,  $E_i$ , RIXS spectra of  $\text{Ca}_3\text{LiOsO}_6$  at 300 K. Four lines are present at  $E < 2$  eV, which are enhanced at  $E_i = 10.874$  keV, whereas the feature at  $E \approx 4.5$  eV is enhanced at  $E_i = 10.878$  keV. This indicates that the  $E < 2$  eV features are intra- $t_{2g}$  excitations, whereas the higher energy feature is from  $t_{2g}$  to  $e_g$  excited states, as has been observed in many  $5d$  oxides (7, 18–20). Subsequent measurements were optimised to probe the  $t_{2g}$  excitations by fixing  $E_i = 10.874$  keV.

Figure 2 presents the detailed RIXS spectra of  $\text{Ca}_3\text{LiOsO}_6$  and  $\text{Ba}_2\text{YO}_6$  at temperatures of 300 K and 6 K. In each spectrum there are 5 peaks in addition to the elastic line: four peaks with  $E < 2$  eV, labeled a, b, c and d (Fig. 2c and d) which we associated with intra- $t_{2g}$  excitations, and a broad peak, e, centered at  $E \sim 4.5$  eV (Fig. 2a and b) associated with  $t_{2g}$  to  $e_g$  excited states. The qualitative similarity of the spectra indicates that these features are not controlled by non-cubic structural distortions, as splittings would be heightened in  $\text{Ca}_3\text{LiOsO}_6$ .

At 300 K the peaks a–d are resolution limited, as determined from least-squares fitting of Gaussian peaks on a flat background to the data, Fig. 2c and d. The peak energies for  $\text{Ca}_3\text{LiOsO}_6$  are  $a_{\text{Ca}} = 0.760(7)$  eV,  $b_{\text{Ca}} = 0.992(5)$  eV,  $c_{\text{Ca}} = 1.470(5)$  eV and  $d_{\text{Ca}} =$

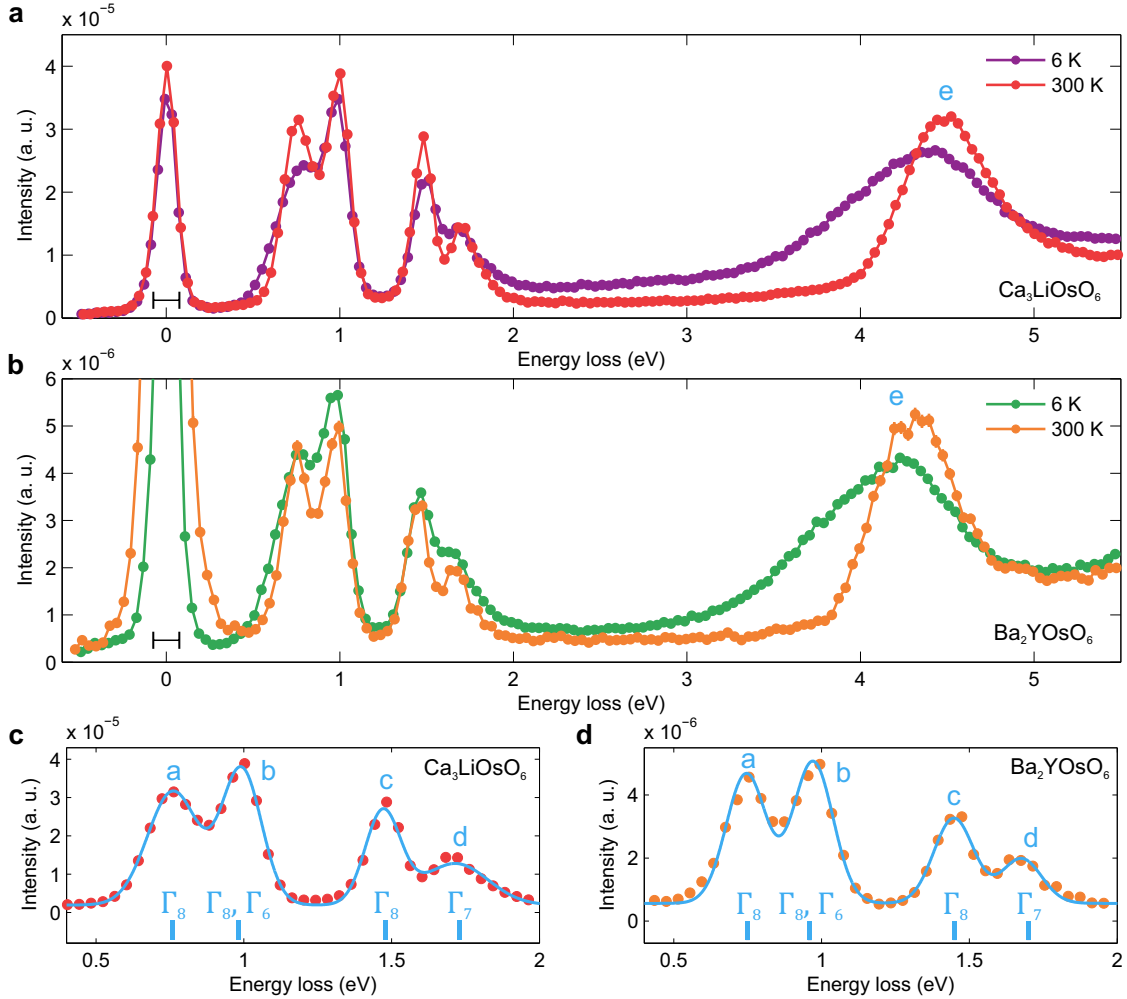


Figure 2: RIXS excitation spectra measured in  $\text{Ca}_3\text{LiOsO}_6$  and  $\text{Ba}_2\text{YOsO}_6$ . Panels a and b show the data for  $\text{Ca}_3\text{LiOsO}_6$  and  $\text{Ba}_2\text{YOsO}_6$ , respectively. Black lines indicate the full-width half maximum of the elastic line. Panels c and d show the energy range 0.4–2 eV, i.e. the  $t_{2g}$  manifold, with the results of Gaussian peak fitting to the data shown as solid lines.

1.72(1) eV, and for  $\text{Ba}_2\text{YOsO}_6$  are  $a_{\text{Ba}} = 0.745(7)$  eV,  $b_{\text{Ba}} = 0.971(7)$  eV,  $c_{\text{Ba}} = 1.447(9)$  eV and  $d_{\text{Ba}} = 1.68(1)$  eV. At 6 K, well below  $T_N$  in both materials, the peaks appear broadened, although maintain the SOC-induced four peak character, see Fig. 2. The low temperature broadening is most pronounced in peak e — this peak is due to 20 different excited levels in the Coulomb plus SOC regime, so no discrete levels can be resolved with current RIXS capabilities. The broadening could be due to splittings from non-cubic structural distortions occurring below the magnetic ordering temperatures - some distortion should be expected from magnetoelastic coupling. However, if a purely structural distortion were the origin we

would expect to see broadening in  $\text{Ca}_3\text{LiOsO}_6$  compared to  $\text{Ba}_2\text{YOsO}_6$  at all temperatures. It is possible that at low temperatures there is dispersion of the levels (17), or that increased hybridisation influences the accessible distribution of excited states — this would be more pronounced for  $e_g$  levels which show greater oxygen overlap. Here, we focus on what the splitting of the  $t_{2g}$  character peaks reveals about the electronic ground state.

The four  $t_{2g}$ -character peaks we observe, Fig. 2, are incompatible with the multiplets expected in standard crystal field theory developed for  $3d$  ions which leads to the  $S=3/2$  ground state (4). Here, we identify that a method first proposed by Kamimura *et al.* (21) for transition metal halides is relevant in this case, in which the assumption that inter-electron interaction energies (including intra- and inter-orbital Coulomb and exchange interactions) are much larger than SOC is dropped (a similar method was also recently derived in Ref. (22)). We identify that such an approach can be utilised to model our TMO RIXS data, with the primary assumption that the hybridisation with the surrounding oxygen ligands leaves the transformation properties of the free ion wavefunctions unaltered. This therefore promotes the breaking of the  $S = 3/2$  singlet and strong entry of SOC. The wavefunctions are therefore described in terms of irreducible representations in the  $O$  double group determined by the octahedral symmetry (4, 23, 24), Fig. 3. This formulation does not necessitate approximations that the cubic crystal field is infinite or that Coulomb or SOC must be neglected, and is not restricted to use for  $5d^3$  configurations (21).

To determine the wavefunctions for the  $5d^3$  case, as in crystal field theory we use initial basis states that describe the ways in which three electrons can occupy the pure  $t_{2g}$  and  $e_g$  levels (i.e. terms such as  $^4A_{2g}$  - which is one electron in each of  $d_{xy}$ ,  $d_{yz}$ ,  $d_{xz}$  with total spin  $3/2$ ), and then apply inter-electron interaction and SOC between these states. The inter-electron interactions are expressed in terms of the Racah parameters  $B$  and  $C$ . Due to hybridisation, the radial form of the  $d$  levels are unknown, i.e.  $B$  and  $C$  deviate from pure ionic values, but the Racah parameters are formulated such that they can be easily extracted from experiment (4, 24, 25). The same interactions can be expressed in terms of intra- and inter-orbital Coulomb interactions,  $U$  and  $U'$ , and the effective Hund's coupling

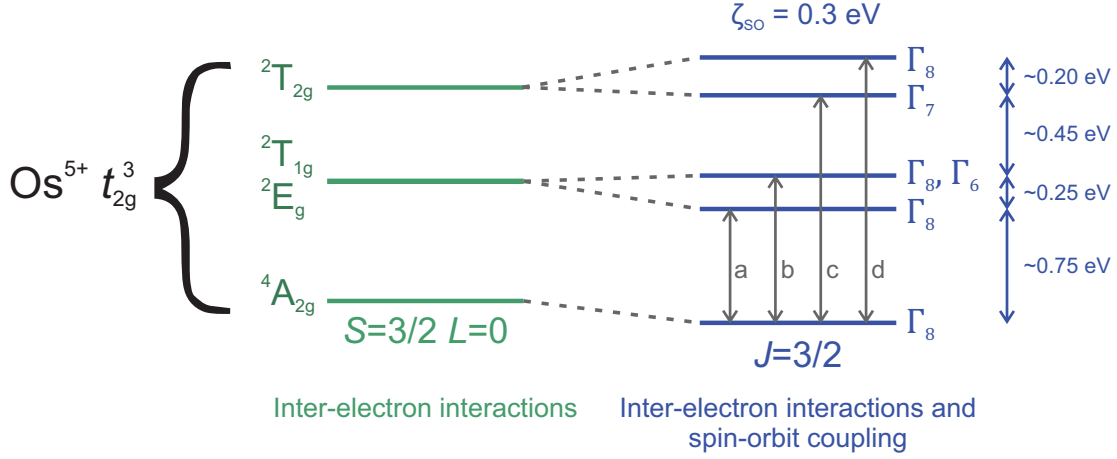


Figure 3: Structure of  $t_{2g}^3$  levels for  $\text{Os}^{5+}$  ions in octahedral environment with strong spin-orbit interaction. The irreducible representations for the states without SOC, i.e.  $\zeta_{\text{SO}} = 0$ , are labeled by the appropriate Mulliken Symbols, full spatial forms are tabulated in many textbooks e.g. Ref. (4). Here  ${}^2E_g$  and  ${}^2T_{2g}$  appear degenerate as we determine  $B = 0.00(4)$  eV within resolution, see main text. The irreducible representations describing the SOC-induced states are four-fold degenerate,  $\Gamma_8$ , and two-fold degenerate,  $\Gamma_6$  and  $\Gamma_7$ . Dashed lines link the final states with the  $\zeta_{\text{SO}} = 0$  states which provide the greatest contribution to them, however each final state is an intermixing of all  $\zeta_{\text{SO}} = 0$  states, which allows SOC to enter the ground state  $\Gamma_8$ . The labels a, b, c and d indicate the excited-state energies that are observed in the RIXS spectra of  $\text{Ba}_2\text{YOsO}_6$  and  $\text{Ca}_3\text{LiOsO}_6$ .

$J_h$ , which have the relationships to the Racah parameters  $J_h = 3B + C$ ,  $U = A + 4B + 3C$  and  $U' = A - 2B + C$  (25). The Racah parameter  $A$ , however, only appears in the diagonal matrix elements of the interactions matrices and causes a constant shift in all eigenvalues, including the ground state, (23, 26) so cannot be determined by the energies of the excited states probed by RIXS. The full interaction matrices are given in Ref. (23). By numerically diagonalising the matrices we determine the eigenstates illustrated in Fig. 3, and are able to fit the resulting eigenvalues to the determined energies  $a_{\text{Ba}} - d_{\text{Ba}}$  and  $a_{\text{Ca}} - d_{\text{Ca}}$ , Fig. 2, see supplementary material for further details. We fix the value of the crystal field to the peak value of peak e,  $10Dq = 4.5$  eV for  $\text{Ca}_3\text{LiOsO}_6$  and  $10Dq = 4.3$  eV for  $\text{Ba}_2\text{YOsO}_6$ , because the positions of levels  $a-d$  are insensitive to small changes in this term, and the resulting levels include negligible mixing of  $e_g$  states, as expected for a strong cubic crystal field splitting.

The resulting parameters provide direct insight into the dominant interactions in the

materials. For  $\text{Ca}_3\text{LiOsO}_6$  we find  $\zeta_{\text{SOC}} = 0.35(7)$  eV,  $B = 0.00(5)$ ,  $C = 0.3(2)$  and  $J_h = 3B + C = 0.3(2)$  eV, and for  $\text{Ba}_2\text{YOsO}_6$  we find  $\zeta_{\text{SO}} = 0.32(6)$  eV,  $B = 0.00(5)$  eV,  $C = 0.3(2)$  eV and  $J_h = 0.3(2)$  eV. The fact that  $\zeta_{\text{SO}}$  is of similar size to  $C$  (and  $J_h$ ) clearly demonstrates that perturbative approaches are not appropriate for the treatment of SOC in  $5d^3$  systems. The ratio of  $C/B$  is commonly used to indicate the scale of deviation from pure ionic wavefunctions (the nephelauxetic effect) by comparison to the same ratio in  $3d$  materials where SOC is weak, with  $C/B = 4$  for  $\text{Cr}^{3+}$  ( $3d^3$ ) ions (4, 24). We find  $B$  to be zero within the error, indicative of a large nephelauxetic effect; improved resolution of RIXS measurements would be advantageous for this comparison. We can, however, look at the eigenvector we determined for the  $\Gamma_8$  ground state - which is a linear combination of the 21 initial basis states which describe 3 electrons occupying the  $t_{2g}$  levels, or two occupying the  $t_{2g}$  levels and one in the  $e_g$  levels (the latter ultimately form a negligible contribution, see supplementary material). The largest component is, as expected, from the  $S = 3/2$   $|^4A_2\rangle$  state, but the next major contribution is from the  $S = 1/2$   $|^2T_{2g}\rangle$  state. For  $\text{Ca}_3\text{LiOsO}_6$  ( $\text{Ba}_2\text{YOsO}_6$ ), these  $|^4A_2\rangle$  and  $|^2T_{2g}\rangle$  terms appear in the normalised eigenvector with weights of 0.95 (0.95) and 0.27 (0.25), respectively — the complete eigenfunctions are given in the supplementary material. This latter component (plus smaller terms) directly explains the entry of SOC physics and the observations of small orbital moments for  $5d^3$  ions (5, 6, 8, 9, 27).

We finally explore how the framework presented provides insight about the physical manifestation of SOC. An x-ray absorption near-edge spectroscopy plus x-ray circular dichroism study of  $5d^3$   $\text{Ir}^{6+}$  double perovskites found strong coupling between orbital and spin moments despite small orbital moments, and suggested this should be due to some deviation from the pure  $t_{2g}^3$  levels (8), with similar results reported in  $\text{Os}^{5+}$  materials (9). The wavefunction we determine explains these results, with a  $J = 3/2$  state which has only a small orbital moment. The observation of a large spin gap in the magnetic excitation spectra of  $\text{Ba}_2\text{YOsO}_6$  and related double perovskites is also explained by the intermediate coupling framework, as the spin gap results from strong SOC-induced anisotropy which is unexplained

in a  $S = 3/2$  picture. In these double perovskites and the pyrochlore  $\text{Cd}_2\text{Os}_2\text{O}_7$  anisotropy is held responsible for stabilisation of the observed magnetic ground states (6, 7, 28). Our results therefore show that intermediate coupling electronic ground states are central in dictating the macroscopic physical properties of such materials. We speculate that a similar approach should be utilised for  $5d^2$  and  $5d^4$  materials, as they are expected to show larger SOC effects (29), alongside increased hybridisation in the  $d^2$  case. The  $d^4$  materials have attracted interest for hosting magnetic order (30) despite the  $d^4$  configuration leading to non-magnetic singlets in either LS or jj limits (29).

### Acknowledgements

We thank A. Huq and M. J. Kirkham for assistance with high-resolution neutron and x-ray diffraction experiments. We thank G. Pokharel for useful discussions. Use of the Advanced Photon Source at Argonne National Laboratory was supported by the U. S. Department of Energy, Office of Science, Office of Basic Energy Sciences, under Contract No. DE-AC02-06CH11357. The research at ORNL's Spallation Neutron Source and High Flux Isotope Reactor was supported by the Scientific User Facilities Division, Office of Basic Energy Sciences, U.S. Department of Energy (DOE). This research was supported in part by the Center for Emergent Materials an National Science Foundation (NSF) Materials Research Science and Engineering Center (DMR-1420451). This research was supported in part by the Japan Society for the Promotion of Science (JSPS) through a Grant-in-Aid for Scientific Research (15K14133, 16H04501). The authors declare no competing financial interests. This manuscript has been authored by UT-Battelle, LLC under Contract No. DE-AC05-00OR22725 with the U.S. Department of Energy. The United States Government retains and the publisher, by accepting the article for publication, acknowledges that the United States Government retains a non-exclusive, paid-up, irrevocable, world-wide license to publish or reproduce the published form of this manuscript, or allow others to do so, for United States Government purposes. The Department of Energy will provide public access to these results of federally sponsored research in accordance with the DOE Public Access



Plan (<http://energy.gov/downloads/doe-public-access-plan>).

---

1. G. Jackeli, G. Khaliullin, *Phys. Rev. Lett.* **102**, 017205 (2009).
2. W. Witczak-Krempa, G. Chen, Y. B. Kim, L. Balents, *Annual Review of Condensed Matter Physics* **5**, 57 (2014).
3. B. J. Kim, *et al.*, *Science* **323**, 1329 (2009).
4. S. Sugano, Y. Tanabe, H. Kamimura, *Multiplets of Transition-Metal Ions in Crystals* (Academic Press, New York and London, 1970).
5. E. Kermarrec, *et al.*, *Phys. Rev. B* **91**, 075133 (2015).
6. A. E. Taylor, *et al.*, *Phys. Rev. B* **93**, 220408 (2016).
7. S. Calder, *et al.*, *Nat Commun* **7**, 11651 (2016).
8. M. A. Laguna-Marco, *et al.*, *Phys. Rev. B* **91**, 214433 (2015).
9. L. S. I. Veiga, *et al.*, *Phys. Rev. B* **91**, 235135 (2015).
10. Y. Shi, *et al.*, *J. Am. Chem. Soc.* **132**, 8474 (2010).
11. G. J. Thorogood, *et al.*, *Dalton Trans.* **40**, 7228 (2011).
12. E. E. Rodriguez, *et al.*, *Phys. Rev. Lett.* **106**, 067201 (2011).
13. Y. Krockenberger, *et al.*, *Phys. Rev. B* **75**, 020404 (2007).
14. S. Calder, *et al.*, *Phys. Rev. Lett.* **108**, 257209 (2012).
15. O. N. Meetei, O. Erten, M. Randeria, N. Trivedi, P. Woodward, *Phys. Rev. Lett.* **110**, 087203 (2013).
16. S. Calder, *et al.*, *Phys. Rev. B* **86**, 054403 (2012).
17. L. J. P. Ament, M. van Veenendaal, T. P. Devereaux, J. P. Hill, J. van den Brink, *Rev. Mod. Phys.* **83**, 705 (2011).
18. X. Liu, *et al.*, *Phys. Rev. Lett.* **109**, 157401 (2012).
19. S. Boseggia, *et al.*, *Phys. Rev. B* **85**, 184432 (2012).
20. M. Moretti Sala, *et al.*, *Phys. Rev. Lett.* **112**, 176402 (2014).
21. H. Kamimura, S. Koide, H. Sekiyama, S. Sugano, *J. Phys. Soc. Jpn.* **15**, 1264 (1960).
22. H. Matsuura, K. Miyake, *J. Phys. Soc. Jpn.* **82**, 073703 (2013).
23. J. C. Eisenstein, *The Journal of Chemical Physics* **34**, 1628 (1961).
24. Brian N. Figgis, M. A. Hitchman, *Ligand field theory and its applications*, Special topics in inorganic chemistry (Wiley, New York, 2000).
25. A. Georges, L. d. Medici, J. Mravlje, *Annual Review of Condensed Matter Physics* **4**, 137 (2013).
26. P. B. Dorain, R. G. Wheeler, *The Journal of Chemical Physics* **45**, 1172 (1966).
27. A. E. Taylor, *et al.*, *Phys. Rev. B* **91**, 100406 (2015).
28. E. V. Kuz'min, S. G. Ovchinnikov, D. J. Singh, *Phys. Rev. B* **68**, 024409 (2003).
29. G. Chen, L. Balents, *Phys. Rev. B* **84**, 094420 (2011).
30. G. Cao, *et al.*, *Phys. Rev. Lett.* **112**, 056402 (2014).
31. T. Gog, *et al.*, *Synchrotron Radiation News* **22**, 12 (2009).
32. M. Wakeshima, Y. Hinatsu, *Solid State Communications* **136**, 499 (2005).
33. B. H. Toby, *J. Appl. Cryst.* **34**, 210 (2001).
34. J. Rodríguez-Carvajal, *Physica B: Condensed Matter* **192**, 55 (1993).
35. C. J. Howard, B. J. Kennedy, P. M. Woodward, *Acta Crystallographica Section B Structural Science* **59**, 463 (2003).

36. J. Kanamori, *Prog. Theor. Phys.* **30**, 275 (1963).
37. M. S. Dresselhaus, G. Dresselhaus, A. Jorio, *Group Theory: Application to the Physics of Condensed Matter* (Springer Berlin Heidelberg, Berlin, Heidelberg, 2008).
38. G. F. Koster, J. O. Dimmock, R. G. Wheeler, H. Statz, *The Properties of the Thirty-Two Point Groups* (The MIT Press, Cambridge (Mass.), 1963).

# Supplementary Material for: Spin-orbit coupling controlled $J = 3/2$ electronic ground state in $5d^3$ oxides

## Resonant inelastic x-ray scattering

RIXS measurements were performed at the Advanced Photon Source (APS) at Sector 27 using the MERIX instrumentation (31). A closed-cycle refrigerator was used to control the sample temperature. The Os  $L_3$ -edge incident energy was accessed with a primary diamond(1 1 1) monochromator and a secondary Si(4 0 0) monochromator. A Si(4 6 6) diced analyzer was used to determine the energy of the beam scattered from the sample, and a MYTHEN strip detector was utilised. All measurements were performed with  $2\theta = 90^\circ$  in horizontal geometry. The RIXS energy resolution was 150 meV FWHM. The raw data counts are normalised to the incident beam intensity via an ion chamber monitor. To compare the temperatures, the 6 K data is normalised so that the featureless energy gain side overlaps with the 300 K data – this accounts for deviations of the beam position on the sample.

## Synthesis

The synthesis route and properties of  $\text{Ca}_3\text{LiOsO}_6$  are reported in Ref. (10). Characterisation of the powder sample utilised here, including diffraction measurements and magnetic structure determination, are reported in Ref. (16). The powder sample of  $\text{Ba}_2\text{YOsO}_6$  of mass 1.5 g was synthesised by grinding together stoichiometric quantities of barium peroxide, yttrium oxide, and osmium metal. The reactants were loaded into an alumina tube which was placed into a silica tube along with a secondary alumina vessel containing  $\text{PbO}_2$ . The silica tube was sealed under dynamic vacuum, and heated to 1000 °C for a period of 48 hours in a box furnace located in a fume hood. The  $\text{PbO}_2$  decomposed into  $\text{PbO}$  at elevated temperature, acting as a source of  $\text{O}_2$  gas for the reaction. A calculated excess was used resulting in  $\frac{1}{4}$  mole excess  $\text{O}_2$  per mole of product in order to ensure full oxidation of the reactants. Care

must be taken when heating Os or Os containing compounds due to the potential formation of highly toxic  $\text{OsO}_4$  gas. X-ray and neutron diffraction and susceptibility measurements were consistent with those previously reported (5), and are detailed in the supplementary material.

### **$\text{Ca}_3\text{LiOsO}_6$ Characterisation**

Polycrystalline  $\text{Ca}_3\text{LiOsO}_6$  was used in this work, for which synthesis route and properties are reported in Ref. (10). Neutron powder diffraction measurements and magnetic structure determination are reported in Ref. (16).

### **$\text{Ba}_2\text{YOsO}_6$ Characterisation**

The temperature dependence of the magnetization of the  $\text{Ba}_2\text{YOsO}_6$  powder was measured with a Quantum Design MPMS SQUID magnetometer. The powder was contained in a gel capsule and mounted in a straw for insertion into the device. Data were collected between 2.5 and 400 K under an applied field of 1 kOe under field cooled (FC) and zero-field cooled (ZFC) conditions. No corrections were applied to the data. A sharp transition at 70 K was observed in both data sets, see Fig.4, associated with the antiferromagnetic ordering of  $\text{Os}^{5+}$  as previously observed(5). The rise of the magnetization at very low temperatures is attributed to the presence of ferromagnetic impurity  $\text{Ba}_{11}\text{Os}_4\text{O}_{24}$ , which has  $T_C = 6.8$  K(32). A Curie-Weiss fit was conducted in the temperature range 300–400 K resulting in a Weiss constant,  $\Theta$ , of -785 K and an effective moment of  $4.27 \mu_B$ . These parameters result in a large frustration index,  $|\Theta/T_N|$ , of 11.2. However, the effective moment is larger than the predicted spin-only moment of  $3.87 \mu_B$  suggesting that the true paramagnetic regime is not achieved below 400 K, consistent with Ref. (5).

### **$\text{Ba}_2\text{YOsO}_6$ Structural Study**

High resolution x-ray and neutron diffraction experiments were performed on  $\text{Ba}_2\text{YOsO}_6$  in an attempt to identify any non-cubic distortion. The synchrotron x-ray experiments

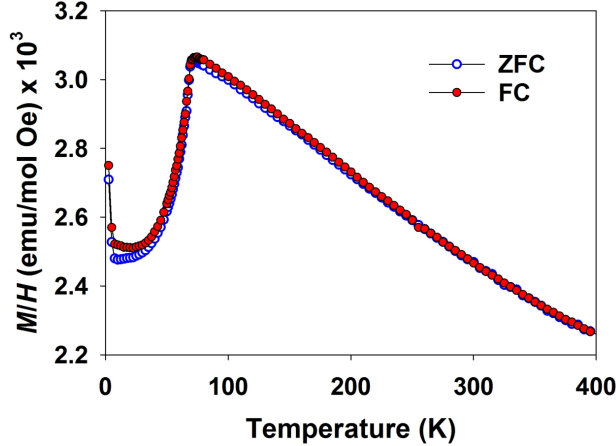


Figure 4: Temperature dependence of the zero field cooled (blue open circles) and field cooled (red closed circles) magnetization of  $\text{Ba}_2\text{YOsO}_6$  under 1 kOe measurement field. The low temperature rise of the magnetization is attributed to the presence of ferromagnetic impurity  $\text{Ba}_{11}\text{Os}_4\text{O}_{24}$ , which has  $T_C = 6.8\text{ K}$ (32).

are optimised for identifying non-cubic lattice parameter splittings, and for identifying Y-Os site mixing, whereas the neutron scattering experiments are more likely to be able to identify distortions and tilting of the oxygen octahedra. Space group  $Fm\bar{3}m$  was used for the refinements, in which the ions are on Wyckoff sites: Ba  $8c$   $(\frac{1}{4}, \frac{1}{4}, \frac{1}{4})$ , Y  $4a$   $(0, 0, 0)$ , Os  $4b$   $(\frac{1}{2}, \frac{1}{2}, \frac{1}{2})$  and O1  $24e$ ,  $(0, 0, z)$ . The Y and Os ions contribute to the same Bragg reflections, therefore for both x-ray and neutron refinements the displacement parameters for these ions were constrained to be equal.

Synchrotron x-ray diffraction measurements were conducted on 11-BM at the Advanced Photon Source with wavelength  $\lambda = 0.4593\text{ \AA}$  at temperature of 295 K. The 0.012 g of sample was mixed with ground quartz in a 1:1 mass ratio to minimize absorption, and this was placed in a 0.4mm radius capillary for the measurement. The data were analyzed via Rietveld refinement as implemented in GSAS(33). Y/Os cation ordering refinements were performed indicating full cation ordering, similar to previous work(5). No non-cubic peak splittings, nor additional peaks, could be identified. The results of refinements based on space group  $Fm\bar{3}m$  is illustrated in Fig.5 and summarized in Table I.

Neutron powder diffraction measurements were conducted on POWGEN at the Spallation Neutron Source at Oak Ridge National Laboratory (ORNL). 1.4 g of  $\text{Ba}_2\text{YOsO}_6$  was

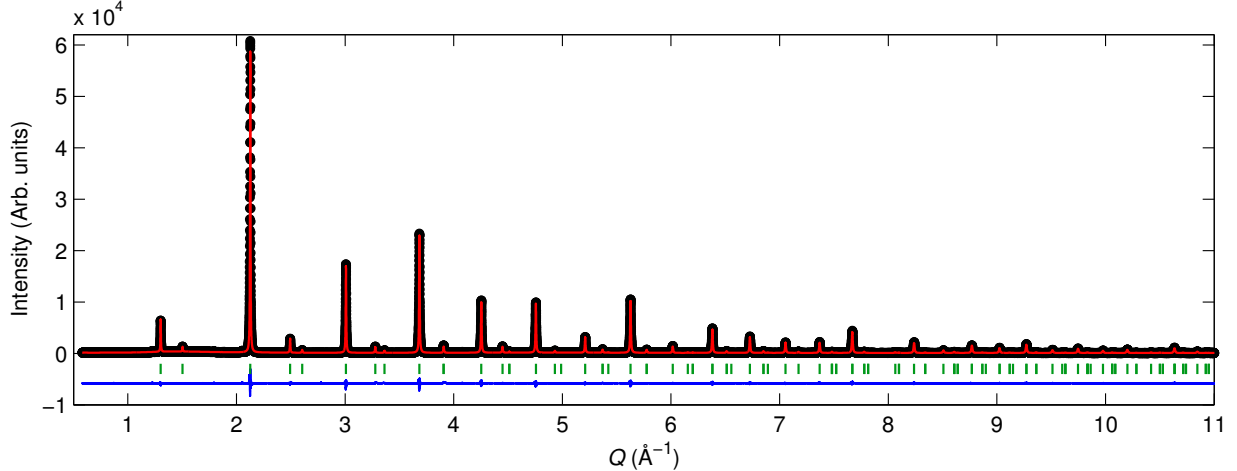


Figure 5: X-ray powder diffraction pattern of  $\text{Ba}_2\text{YOsO}_6$  measured at 295 K. The black circles are observed data, the red line is the calculated pattern, and the blue line is the difference of the two. Allowed reflections of the phase are given as green hashes.

Table I: Results from Rietveld refinements against XRPD data from BM-11 using GSAS. Errors quoted in parenthesis are the standard deviations determined by GSAS.

Temperature	$a(\text{\AA})$	$\chi^2$	$R_{wp}$	O1 $z$	Ba $B_{iso}$	Y/Os $B_{iso}$	O1 $B_{iso}$
295 K	8.35518(1)	2.534	8.75 %	0.2379(2)	0.709(4)	0.248(3)	1.00(3)

contained in a vanadium can, and measured at 10 and 100 K. High-resolution settings were chosen,  $\lambda = 1.066 \text{ \AA}$  and  $f = 60 \text{ Hz}$ , to optimize chances of identifying a non-cubic distortion. The data were analyzed via Rietveld refinement as implemented in Fullprof(34). No peaks associated with octahedral rotations in non-cubic symmetries could be identified(35). The results of refinements based on space group  $Fm\bar{3}m$  is illustrated in Fig.6 and summarized in Table II. In this refinement all ion occupancies were kept at 100 % as indicated by the x-ray data. Using anisotropic displacement parameters for the oxygen positions did not produce an improvement to the fit qualities, so we quote the results with isotropic displacement parameter results for all ions.

Temperature	$a(\text{\AA})$	$\chi^2$	$R_{\text{Bragg}}$	$R_F$	O1 $z$	Ba $B_{iso}$	Y/Os $B_{iso}$	O1 $B_{iso}$
10 K	8.34383(8)	9.91	6.76	3.77	0.23446(5)	0.104(7)	0.107(5)	0.293(6)
100 K	8.34596(8)	10.1	6.83	4.10	0.23438(5)	0.183(7)	0.132(6)	0.342(7)

Table II: Results from Rietveld refinements against NPD data from POWGEN using Fullprof. Errors quoted in parenthesis are the standard deviations determined by Fullprof.

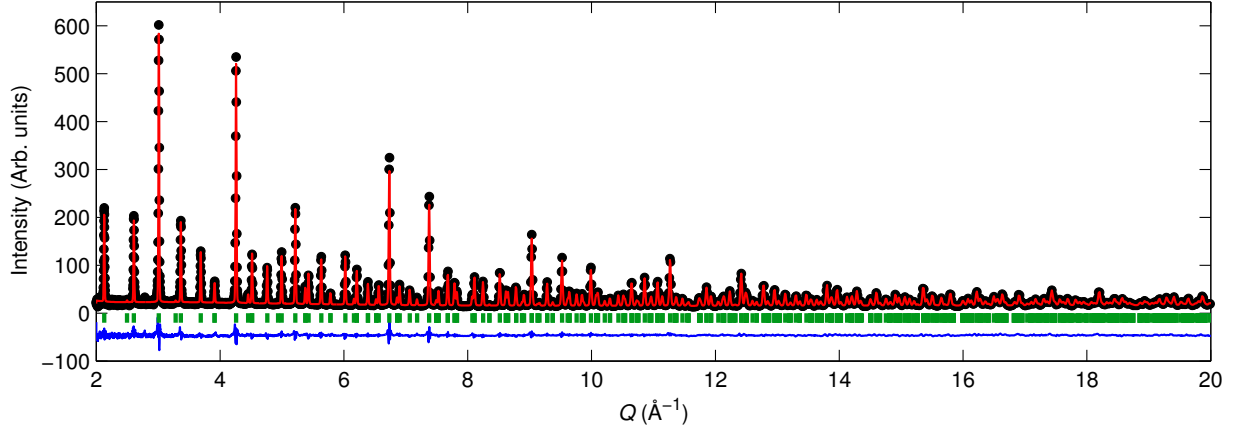


Figure 6: Neutron powder diffraction pattern of  $\text{Ba}_2\text{YOsO}_6$  measured at 10 K. The black circles are observed data, the red line is the calculated pattern, and the blue line is the difference of the two. Allowed reflections of the phase are given as green hashes.

### Spin-Orbit Calculation

As referenced in the main text, the complete Hamiltonian describing cubic-crystal field, Coulomb interactions (including Hund's coupling) and spin-orbit effects is given by Eisenstein(23) in the form of a  $21 \times 21$  matrix for  $\Gamma_8$  and a  $9 \times 9$  matrix for each of the  $\Gamma_6$  and  $\Gamma_7$  representations, describing the interactions between each of the basis states utilized in the standard Coulomb-only model(4, 25, 36). These basis states are the  $|^4A_2\rangle$ ,  $|^2T_{2g}\rangle$  etc. states which describe all the ways in which three electrons can occupy the  $t_{2g}$  and  $e_g$  levels, and are documented in full in textbooks, for example Ref. (4). The interaction matrices are formulated in terms of the Racah parameters,  $A_n$ ,  $B_n$  and  $C_n$  ( $n = 0$  to 4 is symmetry allowed) but we follow the formulation in Ref. (26) and assume only one parameter of each type is required (i.e.  $A_n = A$ ,  $B_n = B$ ,  $C_n = C \forall n$ ) as is commonly adopted(25), and found to be reasonable in Ref. (23) for  $\text{Re}^{4+}$  in Cl octahedra. The term  $A$  is only found on the diagonal elements, adding  $3A$  to each eigenvalue, and therefore the differences in energy between states is independent of  $A$  and we can set it to any arbitrary value in describing our data. We diagonalise the matrices to find the eigenvalues and eigenvectors, and shift all eigenvalues by the energy of the lowest term, so that the ground state is at  $E = 0$ . We then fit the first four excited state eigenvalues to the observed RIXS excitations as described in

the main text.

The basis vectors of the  $\Gamma_8$  representation in the O double group are angular momentum wavevectors  $\phi(J, m_J)$  with  $J = 3/2$  and  $m_J = \frac{3}{2}, \frac{1}{2}, -\frac{1}{2}$  and  $-\frac{3}{2}$  (37, 38). We determine the eigenvector for the  $\Gamma_8$  ground state in terms of a linear combination of 21 basis states describing the three electron occupations of the  $t_{2g}$  and  $e_g$  levels, including  $t_{2g}$ - $e_g$  excited states, although as  $10Dq \sim 4\text{eV}$ , the contributions from these states are extremely small.

The complete normalized eigenfunction of the ground state for  $\text{Ba}_2\text{YOsO}_6$  from a numerical diagonalisation is, to 3 decimal places:

$$\begin{aligned}
|\Gamma_8\text{g.s.}\rangle = & -0.953 |^4A_2(t_{2g}^3)\rangle + 0.069 |^2E_g(t_{2g}^3)\rangle + 0.017 |^2E_g(t_{2g}^2e_g^1)\rangle + 0.015 |^2E_g(t_{2g}^2e_g^1)\rangle \\
& - 0.001 |^2E_g(e^3)\rangle - 0.081 |^2T_{1g}(t_{2g}^3)\rangle - 0.007 |^2T_{1g}(t_{2g}^2e_g^1)\rangle + 0.013 |^2T_{1g}(t_{2g}^2e_g^1)\rangle \\
& - 0.004 |^2T_{1g}(t_{2g}^1e_g^2)\rangle + 0.002 |^2T_{1g}(t_{2g}^1e_g^2)\rangle - 0.024 |^4T_{1g}(t_{2g}^2e_g^1)\rangle \\
& + 0.006 |^4T_{1g}(t_{2g}^1e_g^2)\rangle - 0.007 |^4T_{1g}(t_{2g}^2e_g^1)\rangle - 0.002 |^4T_{1g}(t_{2g}^1e_g^2)\rangle \\
& - 0.252 |^2T_{2g}(t_{2g}^3)\rangle + 0.069 |^2T_{2g}(t_{2g}^2e_g^1)\rangle - 0.013 |^2T_{2g}(t_{2g}^2e_g^1)\rangle \\
& - 0.011 |^2T_{2g}(t_{2g}^1e_g^2)\rangle + 0.006 |^2T_{2g}(t_{2g}^1e_g^2)\rangle - 0.038 |^4T_{2g}(t_{2g}^2e_g^1)\rangle \\
& - 0.098 |^4T_{2g}(t_{2g}^2e_g^1)\rangle.
\end{aligned} \tag{.1}$$

The complete normalized eigenfunction of the ground state for  $\text{Ca}_3\text{LiOsO}_6$  from a numerical diagonalisation is, to 3 decimal places:

$$\begin{aligned}
|\Gamma_8\text{g.s.}\rangle = & -0.947 |^4A_2(t_{2g}^3)\rangle + 0.076 |^2E_g(t_{2g}^3)\rangle + 0.019 |^2E_g(t_{2g}^2e_g^1)\rangle + 0.016 |^2E_g(t_{2g}^2e_g^1)\rangle \\
& - 0.001 |^2E_g(e^3)\rangle - 0.090 |^2T_{1g}(t_{2g}^3)\rangle - 0.007 |^2T_{1g}(t_{2g}^2e_g^1)\rangle + 0.014 |^2T_{1g}(t_{2g}^2e_g^1)\rangle \\
& - 0.004 |^2T_{1g}(t_{2g}^1e_g^2)\rangle + 0.002 |^2T_{1g}(t_{2g}^1e_g^2)\rangle - 0.025 |^4T_{1g}(t_{2g}^2e_g^1)\rangle \\
& + 0.006 |^4T_{1g}(t_{2g}^1e_g^2)\rangle - 0.008 |^4T_{1g}(t_{2g}^2e_g^1)\rangle - 0.002 |^4T_{1g}(t_{2g}^1e_g^2)\rangle \\
& - 0.266 |^2T_{2g}(t_{2g}^3)\rangle + 0.070 |^2T_{2g}(t_{2g}^2e_g^1)\rangle - 0.014 |^2T_{2g}(t_{2g}^2e_g^1)\rangle \\
& - 0.011 |^2T_{2g}(t_{2g}^1e_g^2)\rangle + 0.006 |^2T_{2g}(t_{2g}^1e_g^2)\rangle - 0.038 |^4T_{2g}(t_{2g}^2e_g^1)\rangle \\
& - 0.100 |^4T_{2g}(t_{2g}^2e_g^1)\rangle.
\end{aligned} \tag{.2}$$